

Recover low-frequency for full-waveform inversion via band-limited impedance inversion and projection onto convex sets

Wenyong Pan, Kris Innanen, Gary Margrave, Scott Keating

ABSTRACT

Full-waveform inversion (FWI) provides high-resolution estimates of the subsurface properties by iteratively minimizing a l_2 norm misfit function, which measures the difference between the modelled data and observed data. FWI suffers from cycle-skipping difficulties arising from inaccurate initial models and lack of low frequency information in the seismic data. In this paper, we aim to recover low frequency information from well log data through band-limited impedance inversion. Projection-onto-convex-sets (POCS) algorithms are generally used to infill the missed traces in seismic data reconstruction. In this paper, we also consider recovering the low frequency information by spectral extrapolation with POCS algorithm. The reflectivity estimate is first generated. The frequency spectrum is then extrapolated with POCS algorithm. A band-limited impedance inversion is then performed with the reflectivity section and interpolated well log data. Through this process, we build an enhanced initial model for full-waveform inversion with low frequency information. We then illustrate with numerical examples that the inversion results can be improved with the enhanced initial velocity model.

INTRODUCTION

Full-waveform inversion (FWI) allows for reconstruction of high-resolution velocity models of the subsurface through the extraction of the full information content of the seismic data (Tarantola, 1984; Pratt et al., 1998; Virieux and Operto, 2009). FWI iteratively minimizes a l_2 norm misfit function, which measures the difference between the modelled data and observed data.

FWI is promising but also suffers from many challenges, one of which is cycle-skipping. The inversion process is classically solved with local optimization schemes and is therefore strongly dependent on the starting model definition. It only locates the local global minimum misfit if the starting model is close to the true model. One key assumption and criteria in the localized inversion is that the modelled and observed waveforms are within half a wave-cycle at the lowest frequency to converge iteratively in the right direction. Hence, for successful application of FWI, the modelled data must match the observed data at the lowest usable frequencies within half a wave-cycle. Theoretically, at low frequencies, there is a high chance that the modelled and observed data match within half a wave-cycle. Hence, the low frequencies are crucial to recovering the long wavelength structures of the model.

However, in traditional seismic data, the low frequencies are missed, resulting in FWI applications that are always trapped in local minima. Impedance inversion is very useful for reservoir characterization and band-limited impedance inversion (BLIM) is implemented by incorporating low frequency information from well log data (Ferguson and Margrave, 1996; Lloyd and Margrave, 2013). In this paper, we consider recovering the low frequen-

cies from well log data for full-waveform inversion through band-limited impedance inversion. The impedance inversion result is used as the initial model for full-waveform inversion. However, one problem is that the traces far away from the well log positions may not be reliable. In this paper, we try to recover the low frequency information for the reflectivity section using a projection-onto-convex-sets (POCS) algorithm. The POCS algorithm is generally employed to infill missing seismic data in seismic data reconstruction. In this paper, we attempt to use this method to recover the low frequency information, based on a series of assumptions (Innanen, 2011).

FWI can be carried out in the time domain (Lailly, 1983; Tarantola, 1984; Mora, 1987) or frequency domain (Pratt et al., 1998; Sirgue and Pratt, 2004). When considering computational efficiency, the frequency domain FWI is more attractive because it involves only a set of discrete frequencies for inversion. In this research, we implement frequency domain FWI with a multiscale approach by sequentially increasing the discrete frequencies from low to high (Pratt and Chapman, 1992; Bunks et al., 1995; Sirgue and Pratt, 2004). This multiscale strategy can help to mitigate cycle-skipping problem. The most common frequency selection strategy for this process, the mono-frequency strategy, involves choosing single frequencies for inversion sequentially (Kim et al., 2011).

The gradient in FWI is equivalent to a poorly scaled image, which suffers from geometrical spreading and finite-frequency effects. In Gauss-Newton and full Newton methods for FWI, the search direction can be greatly enhanced by multiplying the gradient with the inverse Hessian. However, the calculation, storage and inversion of the Hessian is extremely expensive. Gradient-based methods (e.g., steepest-descent and non-linear conjugate gradient methods) assume the Hessian matrix is an identity matrix but suffer from slow local convergence rates. Quasi-Newton methods represent alternative strategies for large-scale inverse problems. The quasi-Newton methods do not construct the Hessian explicitly, but update the inverse Hessian approximations by storing the information from previous iterations. The BFGS method, due to Broyden (1970), Fletcher (1970), Goldfarb (1970) and Shanno (1970), is a popular quasi-Newton method used to iteratively approximate the inverse Hessian. The limited-memory BFGS (*l*-BFGS) method stores the changes of the gradient and model from a limited number of previous iterations and uses the stored information to implicitly form an inverse of the approximated Hessian (Nocedal, 1980; Byrd et al., 1995; Nocedal and Wright, 2006). In this research, the *l*-BFGS optimization strategy is adopted and implemented with a "two-loop recursion" scheme (Nocedal and Wright, 2006; Anagaw, 2014; Wu et al., 2015).

The paper is organized as follows. We first review the basic principles of the non-linear least-squares inverse problem. Then, we introduce the flow for the band-limited impedance inversion method and the POCS algorithm. The proposed strategies which combine band-limited impedance inversion and the POCS algorithm are explained. In the numerical section, we first illustrate with numerical examples the effects of cycle-skipping in FWI. Then, we show the effectiveness of the proposed strategies in mitigating the cycle-skipping problem.

THEORY AND METHODS

The non-linear least-squares inverse problem

As a non-linear least-squares optimization problem, FWI seeks to estimate the subsurface parameters by iteratively minimizing the difference between the synthetic data \mathbf{d}_{syn} and observed data \mathbf{d}_{obs} (Lailly, 1983; Tarantola, 1984; Virieux and Operto, 2009; Pan et al., 2015a). The misfit function Φ is formulated in a least-squares form:

$$\Phi(\mathbf{m}) = \frac{1}{2} \sum_{\mathbf{x}_s} \sum_{\mathbf{x}_g} \sum_{\omega} \|\Delta \mathbf{d}(\mathbf{x}_g, \mathbf{x}_s, \omega)\|^2, \quad (1)$$

where $\Delta \mathbf{d} = \mathbf{d}_{obs} - \mathbf{d}_{syn}$ is the data residual vector, and $\|\cdot\|$ denotes the L2 norm. Here, the synthetic data \mathbf{d}_{syn} is related to the seismic wavefield \mathbf{u} by a detection operator \mathcal{P} , which samples the wavefield at the receiver locations: $\mathbf{d}_{syn} = \mathcal{P}\mathbf{u}$. The Newton optimization approach is developed based on the second-order Taylor-Lagrange expansion of the misfit function Φ :

$$\Phi(\mathbf{m} + \Delta \mathbf{m}) \approx \Phi(\mathbf{m}) + \mathbf{g}^\dagger \Delta \mathbf{m} + \frac{1}{2} \Delta \mathbf{m}^\dagger \mathbf{H} \Delta \mathbf{m}, \quad (2)$$

where the symbol " \dagger " indicates the transpose, $\Delta \mathbf{m}$ is the search direction, and $\mathbf{g} = \nabla_{\mathbf{m}} \Phi(\mathbf{m})$ and $\mathbf{H} = \nabla_{\mathbf{m}} \nabla_{\mathbf{m}} \Phi(\mathbf{m})$ indicate gradient and Hessian respectively.

To minimize the quadratic approximation of the misfit function, the updated model at the $(k+1)$ th iteration can be written as the sum of the model at the k th iteration and the search direction $\Delta \mathbf{m}_k$:

$$\mathbf{m}_{k+1} = \mathbf{m}_k + \mu_k \Delta \mathbf{m}_k, \quad (3)$$

where μ_k is the step length, a scalar constant calculated through a line search method satisfying the weak Wolfe condition (Gauthier et al., 1986; Pica et al., 1990; Nocedal and Wright, 2006). Within a Newton optimization framework, the search direction $\Delta \mathbf{m}_k$ is the solution of the Newton linear system:

$$\mathbf{H}_k \Delta \mathbf{m}_k = -\mathbf{g}_k. \quad (4)$$

The gradient is the first-order partial derivative of the misfit function with respect to the model parameter and it indicates the direction in which the misfit function is increasing most rapidly (Pratt et al., 1998). It can be constructed by zero-lag correlation between the Fréchet derivative wavefield with complex conjugate of the data residuals $\Delta \mathbf{d}$:

$$\mathbf{g}(\mathbf{x}) = \nabla_{\mathbf{m}(\mathbf{x})} \Phi(\mathbf{m}) = - \sum_{\mathbf{x}_g} \sum_{\mathbf{x}_s} \sum_{\omega} \Re \left(\frac{\partial \mathbf{d}_{syn}^\dagger(\mathbf{x}_g, \mathbf{x}_s, \omega)}{\partial \mathbf{m}(\mathbf{x})} \Delta \mathbf{d}^*(\mathbf{x}_g, \mathbf{x}_s, \omega) \right), \quad (5)$$

where the symbol "*" denotes the complex conjugate, $\frac{\partial \mathbf{d}_{syn}(\mathbf{x}_g, \mathbf{x}_s, \omega)}{\partial \mathbf{m}(\mathbf{x})}$ indicates the Fréchet derivative wavefield (or Jacobian matrix) recorded at the receiver \mathbf{x}_g due to model perturbation at position \mathbf{x} and $\Re(\cdot)$ denotes the real part. Within the adjoint-state formalism (Plessix, 2006), the gradient can be expressed as (Sirgue and Pratt, 2004; Plessix and Mulder, 2004; Tao and Sen, 2013; Pan et al., 2015a):

$$\mathbf{g}(\mathbf{x}) = \sum_{\mathbf{x}_g} \sum_{\mathbf{x}_s} \sum_{\omega} \Re \left(\omega^2 f_s(\omega) G(\mathbf{x}, \mathbf{x}_s, \omega) G(\mathbf{x}_g, \mathbf{x}, \omega) \Delta \mathbf{d}^*(\mathbf{x}_g, \mathbf{x}_s, \omega) \right), \quad (6)$$

where $G(\mathbf{x}, \mathbf{x}_s, \omega)$ and $G(\mathbf{x}_g, \mathbf{x}, \omega)$ indicate source-side and receiver-side Green's functions respectively. Following equation (6), the gradient can be constructed efficiently by cross-correlating the forward modelled wavefield with the back-propagated data residual wavefield (Virieux and Operto, 2009; Pan et al., 2013, 2014, 2015b). The gradient is poorly-scaled due to geometrical spreading, and it is also contaminated by spurious correlations because of finite-frequency effects and doubly-scattered energy (Pratt et al., 1998). The Hessian operator is the second-order partial derivative of the misfit function with respect to the model parameter (Pratt et al., 1998; Plessix and Mulder, 2004):

$$\begin{aligned} \mathbf{H}(\mathbf{x}, \mathbf{x}') &= \nabla_{\mathbf{m}(\mathbf{x})} \nabla_{\mathbf{m}(\mathbf{x}')} \Phi(\mathbf{m}) \\ &= \sum_{\mathbf{x}_g} \sum_{\mathbf{x}_s} \sum_{\omega} \Re \left(\frac{\partial \mathbf{d}_{syn}^\dagger(\mathbf{x}_g, \mathbf{x}_s, \omega)}{\partial \mathbf{m}(\mathbf{x})} \frac{\partial \mathbf{d}_{syn}^*(\mathbf{x}_g, \mathbf{x}_s, \omega)}{\partial \mathbf{m}(\mathbf{x}')} + \frac{\partial^2 \mathbf{d}_{syn}^\dagger(\mathbf{x}_g, \mathbf{x}_s, \omega)}{\partial \mathbf{m}(\mathbf{x}) \partial \mathbf{m}(\mathbf{x}')} \Delta \mathbf{d}^*(\mathbf{x}_g, \mathbf{x}_s, \omega) \right), \end{aligned} \quad (7)$$

where \mathbf{x}' is the neighboring position around the position \mathbf{x} (Valenciano, 2008; Pan et al., 2015a) and $\frac{\partial^2 \mathbf{d}_{syn}(\mathbf{x}_g, \mathbf{x}_s, \omega)}{\partial \mathbf{m}(\mathbf{x}) \partial \mathbf{m}(\mathbf{x}')}$ means the second-order partial derivative wavefield due to model perturbations at positions \mathbf{x} and \mathbf{x}' . Multiplying the gradient with the inverse Hessian can greatly enhance the model update, which provides a quadratic convergence rate.

Well data regularization

Asnaashari et al. (2013) introduced a prior model norm term for smoothly incorporating prior model information into an FWI workflow. This prior model term can significantly reduce the the inversion sensitivity to incorrect initial conditions. They also studied a dynamic decreasing weighting of the prior model term. Thus, the misfit function can be expressed as:

$$\begin{aligned} \tilde{\Phi}(\mathbf{m}) &= \Phi(\mathbf{m}) + \Phi_w(\mathbf{m}) \\ &= \frac{1}{2} \sum_{\mathbf{x}_s} \sum_{\mathbf{x}_g} \sum_{\omega} \|\Delta \mathbf{d}(\mathbf{x}_g, \mathbf{x}_s, \omega)\|^2 + \lambda \|\mathbf{W}_w(\mathbf{m} - \mathbf{m}_w)\|^2, \end{aligned} \quad (8)$$

where \mathbf{W}_w is the weighting matrix in the model space, \mathbf{m}_w is the well log model and λ is the trade-off parameter for balancing the contribution from the well log model. Thus, the gradient is given as:

$$\nabla_{\mathbf{m}} \tilde{\Phi}(\mathbf{m}) = - \left(\frac{\partial \mathbf{d}_{syn}^\dagger}{\partial \mathbf{m}} \right) \Delta \mathbf{d}^* + \lambda \mathbf{W}_w^\dagger \mathbf{W}_w (\mathbf{m} - \mathbf{m}_w). \quad (9)$$

Band-limited Impedance Inversion

In this section, we introduce the band-limited impedance inversion method, which can be used to invert the seismic data using well log data, providing the low frequencies required by the inversion process (Ferguson and Margrave, 1996). To approximate the impedance of the subsurface imaging using seismic data, it is necessary to account for the band-limited nature of the seismic data, especially at low frequencies.

The normal incidence reflection coefficient is given as:

$$r_j = \frac{I_{j+1} - I_j}{I_{j+1} + I_j}, \quad (10)$$

where r and I indicate the reflection coefficient and impedance respectively. Solving equation (10) for I_{j+1} :

$$I_{j+1} = I_1 \prod_{k=1}^j \frac{1 + r_k}{1 - r_k}, \quad (11)$$

Dividing equation (11) by I_1 and taking the logarithm gives:

$$I_{j+1} = I_1 \exp \left(2 \sum_{k=1}^j r_k \right). \quad (12)$$

If we model the seismic trace as scaled reflectivity: $s_k = \frac{2r_k}{\gamma}$, then equation (12) becomes:

$$I_{j+1} = I_1 \exp \left(\gamma \sum_{k=1}^j s_k \right). \quad (13)$$

Equation (13) integrates the seismic trace and then exponentiates the result to provide an impedance trace.

POCS Algorithm

The POCS algorithm is implemented in an iterative scheme (Innanen, 2011). We suppose that the measure trace $s_0(t)$ is deficient in frequencies below f_0 . The threshold operator Γ_0 is used to generate trace $y_0(t) = \Gamma s_0(t)$. For trace $y_0(t)$, it is equal to $s_0(t)$ for all values above the threshold, and zero everywhere else.

A new spectrum is now generated, equal to $S_0(f)$ within the signal band, and equal to $Y_0(f)$ elsewhere:

$$X_1(f) = \mathcal{H}Y_0(f) + (1 - \mathcal{H})S_0(f), \quad (14)$$

where $\mathcal{H} = H(f - f_0) - H(f + f_0)$ and H is the Heaviside or step function. This spectrum is inverse Fourier transformed to the time domain, forming $s_1(t)$. This process is repeated with a new threshold Γ_1 . The updated trace $s_{k+1}(t)$ is given in terms of $s_k(t)$:

$$s_{k+1}(t) = F^{-1} (\mathcal{H}F (\Gamma_k s_k(t)) + (1 - \mathcal{H})F(s_k(t))), \quad (15)$$

where F and F^{-1} are Fourier and inverse Fourier transforms, respectively.

NUMERICAL EXPERIMENTS

In this numerical section, we first examine the effects of lack of low frequency using the BP velocity model. The BP model has 239×675 grid cells with a grid interval of 10 m in both horizontal and vertical directions. We deploy 67 sources from 100 m to 6700 m with a source interval of 100 m and a depth of 20 m. A total of 675 receivers are distributed from 10 m to 6750 m with a receiver interval of 10 m and a depth of 20 m. A Ricker wavelet with

a 30 Hz dominant frequency is used as the source function. Figures 1a and 1b show the true P-wave velocity model and initial P-wave velocity model respectively. It can be seen that in the initial model, the salt structure, which represents a long wavelength component of the model, has been removed.

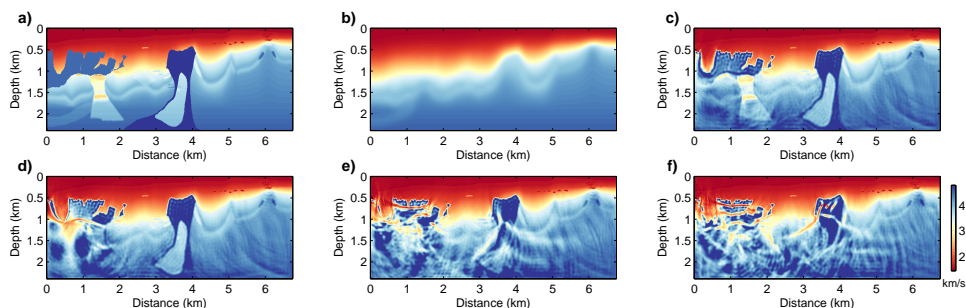


FIG. 1. (a) The true P-wave model; (b) The initial P-wave model; (c) The inverted model with frequency band (1-25 Hz); (d) The inverted model with frequency band (3-25 Hz); (e) The inverted model with frequency band (6-25 Hz); (f) The inverted model with frequency band (8-25 Hz);

Figures 1c, 1d, 1e, 1f show the inversion results with the frequency bands of 1-25 Hz, 3-25 Hz, 6-25 Hz and 8-25 Hz. It can be observed that the salt structures can be reconstructed very well with a frequency band of 1-25 Hz, as shown in Figure 1c. When using a frequency band of 3-25 Hz for inversion, the salt structures can also be recovered, but the sub-salt area within 1-2km can not be inverted. When missing more low frequencies, the salt structures can not be reconstructed very well, as shown in Figures 1e and 1f.

We next illustrate with numerical examples the sensitivity of FWI to the initial model. Figure 2 shows the true Marmousi-II P-wave velocity model. The Marmousi-II model has 244×681 grid cells with a grid interval of 10 m in both horizontal and vertical directions. We deploy 67 sources from 100 m to 6700 m with a source interval of 100 m and a depth of 20 m. A total of 681 receivers are distributed from 10 m to 6810 m with a receiver interval of 10 m and a depth of 20 m.

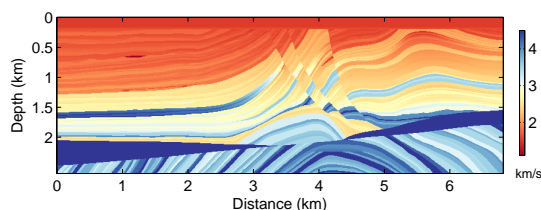


FIG. 2. The true P-wave velocity model.

Figure 3a shows the initial model by smoothing the true model with a Gaussian function. As we can see, this initial model contains long wavelength structure. Figures 3b, 3c and 3d show the inversion results with the frequency bands of 1 Hz-30 Hz, 3 Hz-30 Hz and 6 Hz-30 Hz. It can be observed that the velocity model can be reconstructed very well with the initial model, even if the low frequencies are missing.

Figure 4a shows the linear initial model, which represents a poor starting model for FWI. Figures 4b, 4c and 4d show the inversion results with the frequency bands of 1 Hz-30 Hz, 3 Hz-30 Hz and 6 Hz-30 Hz. We can see that without low frequencies, the model

cannot be reconstructed well. Figure 4e shows the model with well log data interpolation. Figure 4f shows the inversion result with well log data regularization and a frequency band of 6 Hz-30 Hz. Comparing Figure 4d with 4f, we notice that the well data regularization technique can help to mitigate the cycle-skipping difficulty.

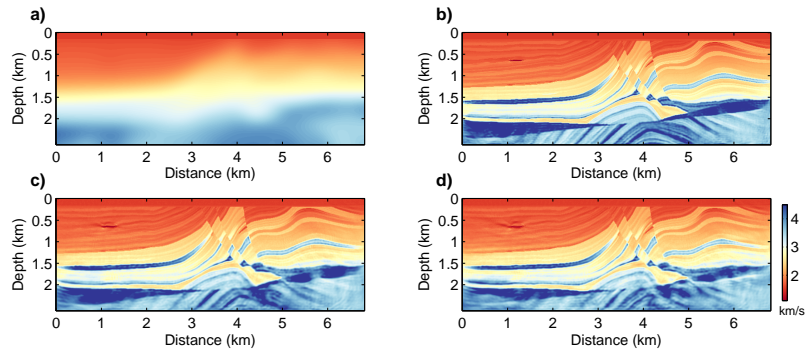


FIG. 3. (a) The smoothed initial P-wave velocity model; (b) The inverted model with frequency band (1 Hz-30 Hz); (c) The inverted model with frequency band (3 Hz-30 Hz); (d) The inverted model with frequency band (6 Hz-30 Hz).

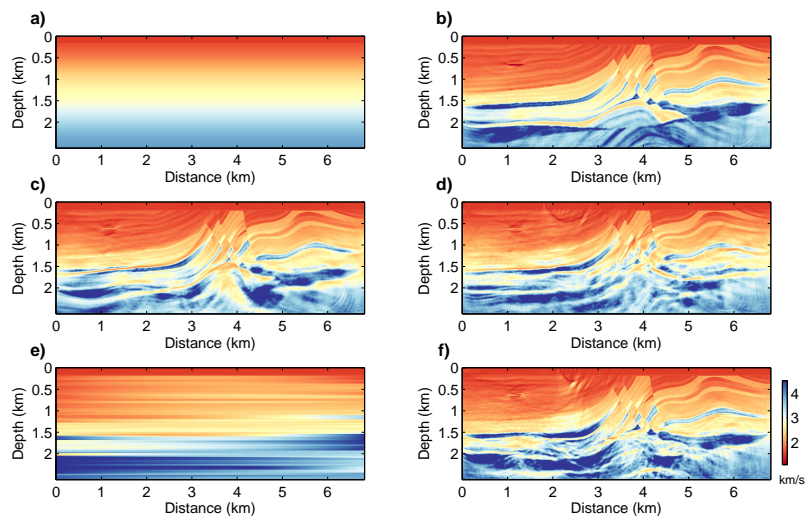


FIG. 4. (a) The linear initial P-wave velocity model; (b) The inverted model with frequency band (1 Hz-30 Hz); (c) The inverted model with frequency band (3 Hz-30 Hz); (d) The inverted model with frequency band (6 Hz-30 Hz); (e) The interpolated model with well log data; (f) The inverted model with well data regularization with frequency band (6 Hz-30 Hz).

Figure 5a shows the initial model obtained using interpolated well log data at 0 km and 6.81 km. Figures 5b, 5c and 5d show the inversion results with the frequency bands of 1-30 Hz, 3-30 Hz and 6-30 Hz respectively. Compared to the inversion results in Figure 4, we observe that the inversion result with the frequency band of 3-30 Hz has been improved, while the inversion result with the frequency band of 6-30 Hz is still not satisfactory.

Figure 6 shows the true reflectivity in time domain. The frequencies below 6 Hz are then removed. The POCS algorithm is then used to recover the low frequencies. The estimated reflectivity section is then used to carry out band-limited impedance inversion combined with the initial model shown in Figure 4a. This process gives an enhanced initial model, as

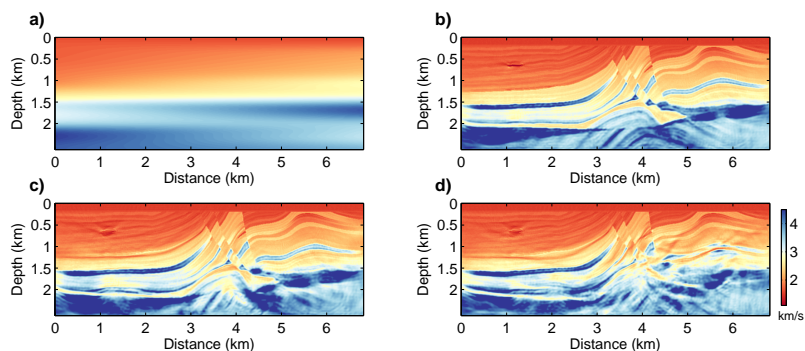


FIG. 5. (a) The initial P-wave velocity model obtained by interpolating the well log data; (b) The inverted model with frequency band (1 Hz-30 Hz); (c) The inverted model with frequency band (3 Hz-30 Hz); (d) The inverted model with frequency band (6 Hz-30 Hz).

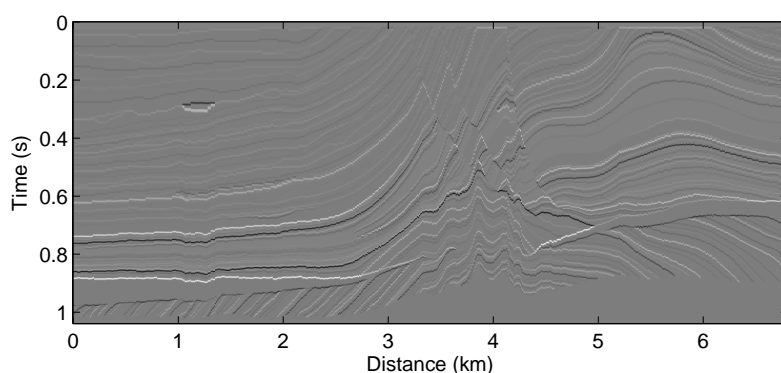


FIG. 6. True reflectivity section in time domain.

shown in Figure 7a. Figures 7b, 7c and 7d show the inverted models with frequency bands of 1-30 Hz, 3-30 Hz and 6-30 Hz respectively. We observe that the inverted model with frequency band of 3-30 Hz becomes much better compared to the ones in Figures 5c and 5d.

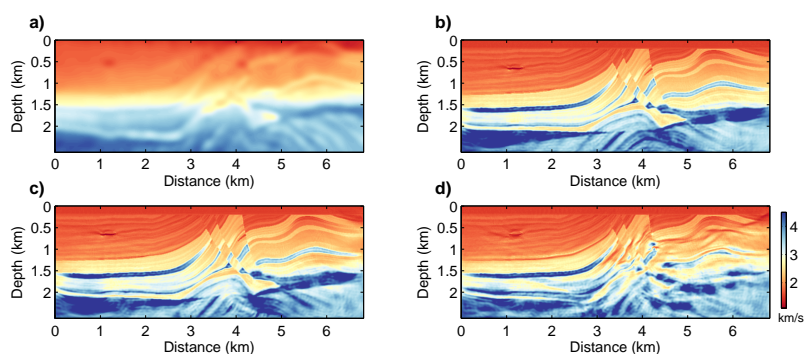


FIG. 7. (a) The initial P-wave velocity model obtained by band-limited impedance inversion and POCS; (b) The inverted velocity model with frequency band (1 Hz-30 Hz); (c) The inverted model with frequency band (3 Hz-30 Hz); (d) The inverted model with frequency band (6 Hz-30 Hz).

CONCLUSION

In this paper, we are trying to recover low frequencies for full-waveform inversion with band-limited impedance inversion combined with a POCS algorithm. We illustrate with

numerical examples that the inversion results can be improved by the proposed strategies. While, more numerical tests are needed for obtaining the reflectivity estimate.

ACKNOWLEDGEMENTS

The authors thank the sponsors of CREWES for continued support. This work was funded by CREWES industrial sponsors and NSERC (Natural Science and Engineering Research Council of Canada) through the grant CRDPJ 461179-13. Author 1 was also supported by a SEG/Chevron scholarship.

REFERENCES

- Anagaw, A. Y., 2014, Full waveform inversion using simultaneous encoded sources based on first and second-order optimization methods: Ph.D. thesis, University of Alberta.
- Asnaashari, A., Brossier, R., Garambois, S., Audebert, F., Thore, P., and Virieux, J., 2013, Regularized seismic full-waveform inversion with prior model information: *Geophysics*, **78**, R25–R36.
- Broyden, C. G., 1970, The convergence of a class of double-rank minimization algorithms: *IMA Journal of Applied Mathematics*, **6**, 222–231.
- Bunks, C., Saleck, F. M., Zaleski, S., and Chavent, G., 1995, Multiscale seismic waveform inversion: *Geophysics*, **60**, 1457–1473.
- Byrd, R. H., Lu, P., and Nocedal, J., 1995, A limited memory algorithm for bound constrained optimization: *SIAM Journal on Scientific and Statistical Computing*, **16**, 1190–1208.
- Ferguson, R. J., and Margrave, G. F., 1996, A simple algorithm for band-limited impedance inversion: CREWES Annual Report, 1–10.
- Fletcher, R., 1970, A new approach to variable metric algorithms: *The Computer Journal*, **13**, 317–322.
- Gauthier, O., Virieux, J., and Tarantola, A., 1986, Two-dimensional nonlinear inversion of seismic waveforms: numerical results: *Geophysics*, **51**, 1387–1403.
- Goldfarb, D., 1970, A family of variable-metric methods derived by variational means: *Mathematics of Computation*, 23–26.
- Innanen, K., 2011, A pocs algorithm for spectral extrapolation: CREWES Annual Report, 1–10.
- Kim, Y., Cho, H., Min, D. J., and Shin, C., 2011, Comparison of frequency-selection strategies for 2D frequency-domain acoustic waveform inversion: *Pure and Applied Geophysics*, **168**, 1715–1727.
- Lailly, P., 1983, The seismic inverse problem as a sequence of before stack migration: *Conference on Inverse Scattering, Theory and Applications*, SIAM, Expanded Abstracts, 206–220.
- Lloyd, H. J. E., and Margrave, G. F., 2013, Investigating the low frequency content of seismic data with impedance inversion: *GeoConvention*, 1–6.
- Mora, P., 1987, Nonlinear two-dimensional elastic inversion of multioffset seismic data: *Geophysics*, **52**, 1211–1228.
- Nocedal, J., 1980, Updating quasi-Newton matrices with limited storage: *Mathematics of Computation*, **35**, 773–782.
- Nocedal, J., and Wright, S. J., 2006, *Numerical Optimization*: Springer.
- Pan, W., Innanen, K. A., and Margrave, G. F., 2013, A comparison of different scaling methods for least-squares inversion/migration: CREWES Annual Report, 1–15.

- Pan, W., Innanen, K. A., Margrave, G. F., and Cao, D., 2015a, Efficient pseudo-Gauss-Newton full-waveform inversion in the τ - p domain: *Geophysics*, **80**, R225–R14.
- Pan, W., Innanen, K. A., Margrave, G. F., Fhler, M. C., Fang, X., and Li, J., 2015b, Estimation of elastic constants in HTI media using Gauss-Newton and Full-Newton multi-parameter full-waveform inversion: SEG Technical Program Expanded Abstracts, 1177–1182.
- Pan, W., Margrave, G. F., and Innanen, K. A., 2014, Iterative modeling migration and inversion (IMMI): Combining full waveform inversion with standard inversion methodology: SEG Technical Program Expanded Abstracts, 938–943.
- Pica, A., Diet, J. P., and Tarantola, A., 1990, Nonlinear inversion of seismic reflection data in a laterally invariant medium: *Geophysics*, **55**, 284–292.
- Plessix, R. E., 2006, A review of the adjoint-state method for computing the gradient of a functional with geophysical applications: *Geophysical Journal International*, **167**, 495–503.
- Plessix, R. E., and Mulder, W. A., 2004, Frequency-domain finite-difference amplitude-preserving migration: *Geophysical Journal International*, **157**, 975–987.
- Pratt, R. G., and Chapman, C. H., 1992, Traveltime tomography in anisotropic media-II. application: *Geophysical Journal International*, **109**, 20–37.
- Pratt, R. G., Shin, C., and Hicks, G. J., 1998, Gauss-Newton and full Newton methods in frequency-space seismic waveform inversion: *Geophysical Journal International*, **133**, 341–362.
- Shanno, D. F., 1970, Conditioning of quasi-Newton methods for function minimization: *Mathematics of Computation*, **24**, 647–656.
- Sirgue, L., and Pratt, R. G., 2004, Efficient waveform inversion and imaging: A strategy for selecting temporal frequencies: *Geophysics*, **69**, 231–248.
- Tao, Y., and Sen, M. K., 2013, Frequency-domain full waveform inversion with plane-wave data: *Geophysics*, **78**, R13–R23.
- Tarantola, A., 1984, Inversion of seismic reflection data in the acoustic approximation: *Geophysics*, **49**, 1259–1266.
- Valenciano, A., 2008, Imaging by wave-equation inversion: Ph.D. thesis, Stanford University.
- Virieux, A., and Operto, S., 2009, An overview of full-waveform inversion in exploration geophysics: *Geophysics*, **74**, WCC1–WCC26.
- Wu, S., Wang, Y., Zheng, Y., and Chang, X., 2015, Limited-memory BFGS based least-squares pre-stack Kirchhoff depth migration: *Geophysical Journal International*, **202**, 738–747.